PAPER

Check for updates

All near-infrared multiparametric luminescence thermometry using Er^{3+}, Yb^{3+}-doped YAG nanoparticles†

Jovana Periša,[a] Zoran Ristić,[a] Wojciech Piotrowski, [b] Željka Antić, [a] Lukasz Marciniak [b] and Miroslav D. Dramićanin *[a]

This paper presents four new temperature readout approaches to luminescence nanothermometry in spectral regions of biological transparency demonstrated on Yb^{3+}/Er^{3+}-doped yttrium aluminum garnet nanoparticles. Under the 10 638 cm^{-1} excitation, down-shifting near infrared emissions (>10 000 cm^{-1}) are identified as those originating from Yb^{3+} ions' $^2F_{5/2} \rightarrow {}^2F_{7/2}$ (~9709 cm^{-1}) and Er^{3+} ions' $^4I_{13/2} \rightarrow {}^4I_{15/2}$ (~6494 cm^{-1}) electronic transitions and used for 4 conceptually different luminescence thermometry approaches. Observed variations in luminescence parameters with temperature offered an exceptional base for studying multiparametric temperature readouts. These include the temperature-dependence of: (i) intensity ratio between emissions from Stark components of Er^{3+} $^4I_{13/2}$ level; (ii) intensity ratio between emissions of Yb^{3+} ($^2F_{5/2} \rightarrow {}^2F_{7/2}$ transition) and Er^{3+} ($^4I_{13/2} \rightarrow {}^4I_{15/2}$ transition); (iii) band shift and bandwidth and (iv) lifetime of the Yb^{3+} emission ($^2F_{5/2} \rightarrow {}^2F_{7/2}$ transition) with maximal sensitivities of 1% K^{-1}, 0.8% K^{-1}, 0.09 cm^{-1} K^{-1}, 0.46% K^{-1} and 0.86% K^{-1}, respectively. The multimodal temperature readout provided by this material enables its application in different luminescence thermometry setups as well as improved the reliability of the temperature sensing by the cross-validation between measurements.

Introduction

Luminescence thermometry may be exploited in many environments where other thermometry methods fail. It has prospective applications at cryogenic temperatures, in extremely high temperature settings, and even in harsh environments. It can be incredibly useful in the biomedical field since temperature plays a critical role in determining dynamics and properties of any biosystem.[1] In medicine, the precise knowledge of tissue temperature is crucial for novel cancer treatments based on the induced heating of malignant cells.

Still, in biological systems, it is quite difficult to assess noninvasively inter- or intra-cellular temperature by common thermometers. Temperature measurements based on the changes in luminescent properties of nanomaterials are considered as a promising route to meet these needs. As the temperature of the nanomaterial changes, its luminescence features such as emission intensity, decay and rise time, spectral band positions and bandwidths, spectral shapes, an

emission polarization, may change, thus providing many different routes for remote temperature sensing. The readers are referred to several review and research articles for more information on the topic of luminescent nanothermometry[2–6] and its biological applications.[7–9]

Besides the requirement of accurate distinguishing temperature fluctuations with thermal resolution below 1 K over a narrow temperature range (303 K–333 K), there are some additional constraints regarding the material considered for application in the biological systems. The light absorbance and scattering by tissue create limitations that need to be alleviated to ensure accurate and reliable temperature detection.[10–13] Thus, the near-infrared (NIR) luminescence within the biological transparency windows (BW I: 15 385–10 526 cm^{-1}; BW II: 10 000–7407 cm^{-1}; BW III: 6667–5405 cm^{-1}), where light has its maximum depth of penetration in the tissue, is highly desirable to ensure the measurement accuracy.[14,15]

The ideal scenario for luminescence nanothermometry in the biological systems is the utilization of the all-NIR nanothermometers that can be excited in BW I and emit in BW II and/or BW III.[14,16–22] Compared to traditional ones, these nanothermometers show several benefits that are reflected in the possibility of contactless, fast, and non-invasive temperature measurement, high spatial resolution and sensitivity, and simple luminescence signal detection.[23–28]

Because of their numerous advantages such as the presence of thermally coupled levels, long emission lifetimes, narrow

[a]*Vinča Institute of Nuclear Sciences – National Institute of the Republic of Serbia, University of Belgrade, P.O. Box 522, Belgrade 11001, Serbia. E-mail: dramican@vinca.rs*

[b]*Institute of Low Temperature and Structure Research, Polish Academy of Sciences, Okólna 2, 50-422 Wroclaw, Poland*

emission bands and resilience to photodegradation, the lanthanide-doped inorganic materials are the most used type of thermographic phosphors.[29–32] Among lanthanide dopants, erbium (Er^{3+}) ion is a promising candidate for *in vivo* luminescence thermometry due to its intense emission in the spectral range that overlaps within BW I and BW III and absorption band in the BW I. However, the relatively low absorption cross-section of Er^{3+} in the BW I result in a weak emission efficiency. Therefore, to circumvent this limitation the Yb^{3+} co-dopant can be used, which is well known for its high absorption cross section at 10 638 cm^{-1} as a sensitizer of Er^{3+} NIR luminescence.[25,33–36]

For this study, we have prepared luminescent nano-thermometers based on yttrium aluminium garnet ($Y_3Al_5O_{12}$, YAG) nanocrystals doped with Yb^{3+} and Er^{3+} using the modified Pechini method.[37–39] YAG is well-known host material which possess high photo resistance, chemical stability, and ease of emission tuning.[40]

So far, Er^{3+} activated materials have been extensively used for the ratiometric luminescence thermometry in the visible spectral region which utilize the green emissions from $^2H_{11/2} \rightarrow {}^4I_{15/2}$ and $^4S_{3/2} \rightarrow {}^4I_{15/2}$ transitions[25] with several recent attempts to exploit the intensity ratio of the blue $^4F_{7/2} \rightarrow {}^4I_{15/2}$ and green $^4S_{3/2} \rightarrow {}^4I_{15/2}$ emissions for higher sensitivity.[5] The thermometry uses of the Er^{3+} emissions from thermally coupled excited levels in the near-infrared has only recently demonstrated by exploiting the ratio of $^2H_{11/2} \rightarrow {}^4I_{13/2}$ and $^4S_{3/2} \rightarrow {}^4I_{13/2}$ weak emissions in BW-I.[14,41]

The aim of this work was to investigate four completely new NIR temperature readouts based on Er^{3+} and Yb^{3+} emissions in BW-II excited by 10 638 cm^{-1} radiation (BW I) over the wide temperature range (80–600 K). These include approaches to thermometry which exploit temperature-dependence of: (i) emission intensity ratio between Stark components of Er^{3+} $^4I_{13/2}$ level ($^4I_{13/2} \rightarrow {}^4I_{15/2}$ transition) in the BW III; (ii) emission intensity ratio between emissions of Yb^{3+} ($^2F_{5/2} \rightarrow {}^2F_{7/2}$ transition) in the BW II and Er^{3+} ($^4I_{13/2} \rightarrow {}^4I_{15/2}$ transition) in the BW III; (iii) band shift, (iv) bandwidth and (v) lifetime of the Yb^{3+} emission ($^2F_{5/2} \rightarrow {}^2F_{7/2}$ transition, BW II).

Materials and methods

Chemicals and samples synthesis

Herein, three samples with the following formula: $Y_{2.7}Yb_{0.3}Al_5O_{12}$ (YAG:10Yb), $Y_{2.67}Yb_{0.3}Er_{0.03}Al_5O_{12}$ (YAG:10Yb1Er), $Y_{2.64}Yb_{0.3}Er_{0.06}$-$Al_5O_{12}$ (YAG:10Yb2Er) were synthesized *via* modified Pechini method. Metal nitrates (yttrium(III) nitrate hexahydrate, $Y(NO_3)_3 \times 6H_2O$; ytterbium(III) nitrate pentahydrate, $Yb(NO_3)_3 \times 5H_2O$; erbium(III)-nitrate pentahydrate, $Er(NO_3)_3 \times 5H_2O$; aluminium(III) nitrate nonahydrate, $Al(NO_3)_3 \times 9H_2O$; Alfa Aesar, purity 99.9%, 99.9%, 99.99+, 98+%, respectively); citric acid – CA ($HOC(COOH)(CH_2COOH)_2$, Sigma Aldrich, ACS reagent, ≥99.5%) and ethylene glycol – EG ($HOCH_2CH_2OH$, Sigma Aldrich, anhydrous, 99.8%) were used as starting materials without further purification.

In a typical procedure, calculated amounts of metal nitrate precursors were added to the solution of citric acid in ethylene glycol (M : CA : EG = 1 : 5 : 25) and stirred at 353 K for 30

minutes. After increasing temperature to 493 K, stirring was continued until the brownish gel was obtained. The obtained gels were transferred into the alumina crucible and placed into the furnace at 873 K for 2 hours, followed by annealing at 1373 K for 2 hours. The powder samples obtained after the annealing were cooled down to room temperature and ground in a mortal.

Characterisation methods and instrumentation

Crystal structure of the powder was studied by X-ray diffractometer (XRD) from Rigaku SmartLab (Cu-Kα1, 2 radiation, λ = 0.1540 nm) at room temperature. The measurement was recorded over the $10°$–$90°$ 2θ-range, with $0.02°$ step size and $1°$ min^{-1} counting time. Relevant results of the structural analysis were obtained using built-in PDXL2 package software. The morphology of the samples was characterized by a field emission gun TESCAN MIRA3 scanning electron microscope. Before the observation, the samples were coated with a thin layer of Au using a standard sputtering technique (Polaron SC502 – Fison Instruments, UK). Diffuse reflectance spectral measurements were performed on the Thermo Evolution 600 spectrometer equipped with an integrated sphere, using $BaSO_4$ as a blank. Transmission electron microscope images were obtained using a TEM Philips CM-20 SuperTwin operating at 160 kV with an optical resolution of 0.25 nm. The temperature of the sample was controlled using a THMS 600 heating–cooling stage from Linkam (0.1 K temperature stability and 0.1 K set point resolution). The temperature range in which both the temperature-dependent emission spectra and luminescent lifetime were recorded was from 80 K to 600 K. The emission spectra were measured using the 10 638 cm^{-1} (940 nm) excitation line from a laser diode (LD) and a FLS1000 Fluorescence Spectrometer from Edinburgh Instruments (0.1 nm spectral resolution). Luminescence decay profiles were recorded using FLS1000 Fluorescence Spectrometer from Edinburgh Instruments with μFlash lamp as an excitation source and the signal was detected using a R928P side window photomultiplier tube from Hamamatsu. Temperature-dependent luminescent lifetime was controlled using the above-mentioned heating-cooling stage from Linkam.

Luminescence thermometry

Temperature-dependant (80–600 K) photoluminescent emission measurements are performed under 10 638 cm^{-1} excitation (BW I) in both steady-state (10 000–6250 cm^{-1} spectral range; BW II and III) and time-resolved domain (emission decays recorded around 9709 cm^{-1}, BW II). The observed variations of luminescence with temperature offer an exceptional base for studying the multiple temperature readouts. To describe the quality and potential use of thermometer the important quantities of absolute (S_A) and relative sensitivity (S_R) are introduced as:

$$S_A = \left| \frac{\partial Q}{\partial T} \right|, \tag{1}$$

$$S_R = \frac{100\%}{Q} \left| \frac{\partial Q}{\partial T} \right|. \tag{2}$$

where Q represents the thermometric parameter of interest (lifetime, LIR, bandshift, and bandwidth).

The luminescence intensity ratio (LIR), the most frequently exploited luminescent thermometry temperature readout method, was tested both by using high and low energy Stark components of Er^{3+} emission or by using the combination of Yb^{3+} and Er^{3+} emissions.

The first temperature indicator $LIR_{Er/Er}$ is defined as the ratio of integrated emission intensities from high-energy and low-energy emissions of the Er^{3+} $^4I_{13/2} \rightarrow {}^4I_{15/2}$ transition that should obey Boltzmann law:

$$Q = LIR_{Er/Er} = \frac{I_{Er}^{high}}{I_{Er}^{low}} = B \times \exp\left(-\frac{\Delta E}{kT}\right). \quad (3)$$

here, ΔE represents the average energy difference between two groups states in question, B is a constant that depends on values of radiative transition probabilities, energies of emission barycenters and degeneracies of energy levels involved, and k is the Boltzmann constant. Alternatively, this equation can be shown in the form where there is linear dependence between $\ln(LIR_{Er/Er})$ and inverse temperature:

$$\ln(LIR_{Er/Er}) \propto -\frac{\Delta E}{k} \frac{1}{T}. \quad (4)$$

Based on eqn (1)–(3), the values of S_A and S_R are then calculated.

On the other hand, for the other LIR that utilizes both Yb^{3+} and Er^{3+}, Boltzmann model emissions is not applicable, thus a semi empirical approach is applied to characterize thermometer performance.

Readouts based on the temperature-induced variations in the band-shift and bandwidth can be described and fitted by integral equations proposed by McCumber and Sturge[42] and Yen et al.:[43]

$$\delta E(T) \, [cm^{-1}] = \alpha \left(\frac{T}{\theta_D}\right)^4 \int_0^{\frac{\theta_D}{T}} \frac{t^3}{e^t - 1} dt, \quad (5)$$

$$\Delta E(T) \, [cm^{-1}] = E^{inh} + \bar{\alpha} \left(\frac{T}{\theta_D}\right)^7 \int_0^{\frac{\theta_D}{T}} \frac{t^6 e^t}{(e^t - 1)^2} dt. \quad (6)$$

In the equations above, θ_D represents the Debye temperature of the host material, $t = \theta_D/T$, α and $\bar{\alpha}$ are the electron–phonon coupling coefficients for the line-shift and line-broadening, respectively, and E^{inh} is the value of the inhomogeneous linewidth.

Finally, emission lifetime was used on Yb^{3+} line as another read out approach to temperature sensing. Since the standard formulas for lifetime quenching with temperature[44,45] cannot describe the temperature behaviour in these samples, a semi-empirical approach is proposed to fit the experimental data.

Results and discussion

Structural and morphological characterization

X-ray powder diffraction patterns of the YAG:10Yb, YAG:10Yb1Er and YAG:10Yb2Er samples presented in Fig. 1a correspond to body-centred cubic structure with $Ia\bar{3}d$ (230)

space group (ICDD card no. 01-073-3184). No other phases were detected indicating that the Yb^{3+} and Er^{3+} dopant ions have been effectively incorporated into the YAG host lattice due to the equal valence (+3) and similar ionic radii between the Y^{3+} (0.107 nm) and Yb^{3+} (0.104 nm) and Er^{3+} (0.106 nm) ions.[46] Additionally, the Rietveld refinement method was used to determine mean crystallite size of powder particles and the relevant structural parameters. The starting parameters for the analysis were taken according to the ref. 47 and the results are summarized in Table S1 in the ESI.†

Scanning electron microscopy was performed to investigate surface morphology and micrographs of the representative YAG:10Yb1Er sample taken under different magnifications are shown in Fig. 1b–d. At the micron-level, the morphology of representative sample appears as a combination of different size chunks, while at the nano-level it is clearly visible that the chunks are dense and composed of spherical particles bellow 50 nm in size.

Fig. 1e–g show transmission electron microscopy images of the YAG:10Yb1Er sample recorded under different magnifications, along with the histogram showing particle size distribution (Fig. 1h). The powder consists of a sphere-like shaped nanoparticles of 35 nm in diameter on average.

UV-vis-NIR diffuse reflectance spectra of YAG:10Yb, YAG:10Yb1Er and YAG:10Yb2Er powder samples recorded at room temperature are presented in Fig. 1i. The absorption bands in the short wavelength range correspond to the Er^{3+} absorptions from the $^4I_{15/2}$ level to different excited levels: $^4G_{11/2}/^4G_{9/2}$ (26 525 cm^{-1}), $^4F_{3/2}/^4F_{5/2}$ (22 173 cm^{-1}), $^4F_{7/2}$ (20 534 cm^{-1}), $^2H_{11/2}$ (19 048 cm^{-1}), $^4S_{3/2}$ (18 484 cm^{-1}) $^4F_{9/2}$ (15 267 cm^{-1}), $^4I_{9/2}$ (12 690 cm^{-1}). The absorption band visible at the long wavelengths, from 10 870 to 9524 cm^{-1} is due to the Yb^{3+} $^2F_{7/2} \rightarrow {}^2F_{5/2}$ transition.[48–50] Considering that the BW I end at 10 526 cm^{-1}, YAG : Yb^{3+}, Er^{3+} can be effectively excited with 10 638 cm^{-1} radiation without heating the biological environment.[51]

Temperature readout using the intensity ratio of emissions from high and low energy Stark components of Er^{3+}

Fig. 2a shows the normalized emission band from Er^{3+} $^4I_{13/2} \rightarrow {}^4I_{15/2}$ transition that spans 6200–7000 cm^{-1} measured over the 80–600 K range under 10 638 cm^{-1} excitation (YAG:10Yb1Er sample). This band comprises emissions from multiple transitions between 7 high-energy Stark components of $^4I_{13/2}$ level and 8 low-energy Stark components of $^4I_{15/2}$ level, Fig. 2b.

Fig. 2c shows experimental results obtained for YAG:10Yb1Er and YAG:10Yb2Er samples while Fig. 2d presents the $\ln(LIR_{Er/Er})$ vs. $1/T$ plot in the temperature range where experimental data follow the Boltzmann distribution relation ($T > 160$ K). Based on the linear fit to eqn (4) (dashed lines in Fig. 2d), ΔE of 192 cm^{-1} and 196 cm^{-1} were obtained for the YAG:10Yb1Er and YAG:10Yb2Er samples, respectively. The obtained ΔE values are in good agreement with the energy separation between low and high energy $^4I_{13/2}$ Stark levels.[52]

For the $LIR_{Er/Er}$ in the temperature range where the thermalization is a dominant thermally dependent process responsible for the intensity ratio changes, S_A and S_R can be
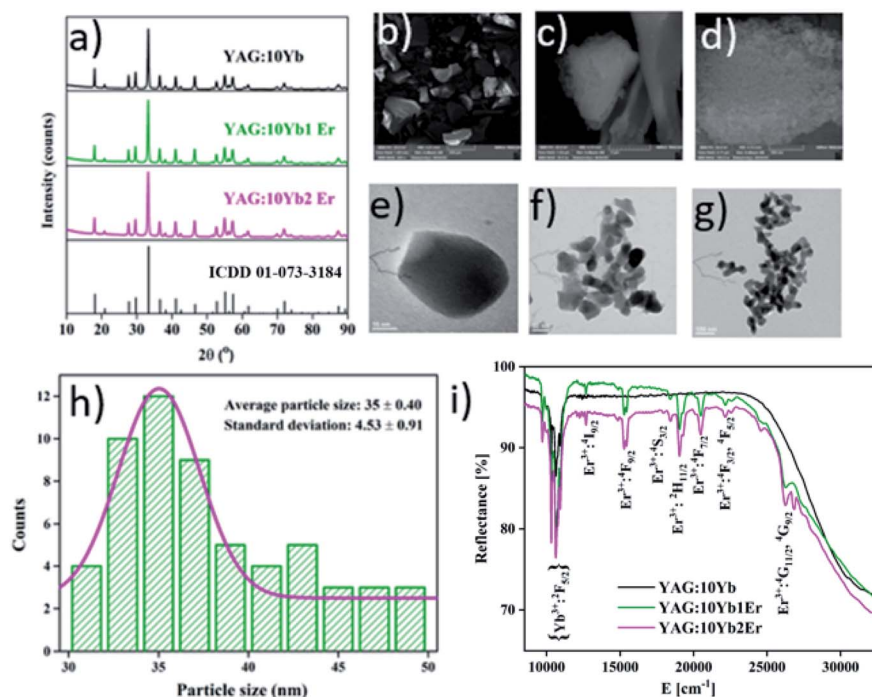
Fig. 1 (a) X-ray diffraction patterns of YAG:10Yb, YAG:10Yb1Er and YAG:10Yb2Er samples. The diffraction peaks are indexed according to the ICDD card no. 01-073-3184. (b)–(d) Scanning electron microscopy images of the representative YAG:10Yb1Er sample recorder under 200×, 30 000× and 100 000× magnification, respectively. (e)–(g) Transmission electron microscopy images of the representative YAG:10Yb1Er sample showing the sphere and sphere-like shaped particles with aggregation tendency. (h) Particle size distribution histogram. (i) Diffuse reflectance spectra of YAG:10Yb, YAG:10Yb1Er and YAG:10Yb2Er samples.
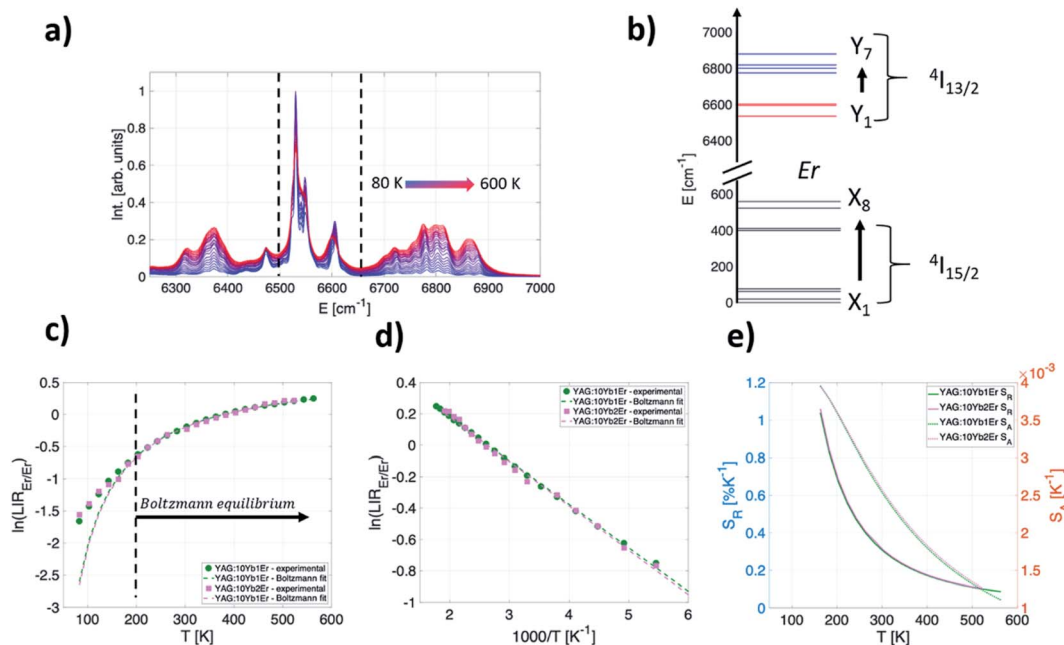

Fig. 2 (a) Part of the temperature-dependant (80–600 K) photoluminescence emission spectra of representative YAG:10Yb1Er sample and (b) Stark energy diagram. Thermometric properties of YAG:10Yb1Er (green) and YAG:10Yb2Er (pink) samples: (c) experimental (symbols) and theoretical (full line) temperature-dependent luminescence intensity ratio in logarithmic scale; (d) the $\ln(\mathrm{LIR}_{\mathrm{Er/Er}})$ vs. $1/T$ plot and (e) S_A and S_R for the $\mathrm{LIR}_{\mathrm{Er/Er}}$ readout.

calculated from eqn (1)–(3). As seen from their graphical representation (Fig. 2e), both absolute and relative sensitivities decrease with temperature with the highest S_A and S_R values of approximately 4×10^{-3} K^{-1} and 1% K^{-1} at 160 K for both samples.

Therefore, this temperature readout provides excellent sensitivity for low-temperature measurements. In the physiological relevant temperature range (303–333 K), the readout shows moderate relative sensitivity of around 0.3% K^{-1} at 310 K.

Temperature readout using the intensity ratio of Yb^{3+} and Er^{3+} emissions

Photoluminescent emission spectra of YAG:10Yb1Er and YAG:10Yb2Er samples recorded in 80–600 K temperature range are presented in Fig. 3a and b. Under the 10 638 cm^{-1} excitation (BW I), emissions are identified as those originating from the $^2F_{5/2} \rightarrow {}^2F_{7/2}$ electronic transition of Yb^{3+} (around 9710 cm^{-1}, BW II, I_{Yb}) and the $^4I_{13/2} \rightarrow {}^4I_{15/2}$ of Er^{3+} (around 6494 cm^{-1}, BW III, I_{Er}).

The second thermometric parameter considered in this work, LIR$_{Yb/Er}$, utilizes their emission intensities ratio defined as:

$$Q = \mathrm{LIR}_{Yb/Er} = \frac{I_{Yb}}{I_{Er}}. \tag{7}$$

The experimentally obtained LIR$_{Yb/Er}$ values for both samples are presented in Fig. 3c while the temperature dependences of the individual emissions are given in the ESI (Fig. S1†). For calibration, a semiempirical quadratic equation

is found as the most suitable for the fitting of ln(LIR$_{Yb/Er}$) vs. T dependence (dashed lines on Fig. 3c):

$$\ln(\mathrm{LIR}_{Yb/Er}) = a_1 T^2 + a_2 T + a_3, \tag{8}$$

where a_1, a_2 and a_3 are the fitting parameters ($a_1 = 4.8 \times 10^{-6}$ K^{-2}, $a_2 = -8.1 \times 10^{-3}$ K^{-1}, $a_3 = 1.31$ and $a_1 = 6.1 \times 10^{-6}$ K^{-2}, $a_2 = -9.0 \times 10^{-3}$ K^{-1}, $a_3 = 1.11$, for YAG:10Yb1Er and YAG:10Yb2Er samples, respectively). For the temperature dependence described by eqn (8), S_A and S_R are obtained using eqn (1) and (2) (Fig. 3d).

The interesting point to highlight here is that the LIR$_{Yb/Er}$ is applicable in the whole investigated temperature range from cryogenic temperatures (80 K) up to remarkably high temperatures (600 K) with both S_A and S_R reaching the highest values at cryogenic temperatures. The maximum relative sensitivity of 0.8% K^{-1} at 80 K is obtained for the YAG:10Yb2Er sample. In the physiological relevant temperature range (303–333 K), this readout also shows moderate relative sensitivity of around 0.5% K^{-1} at 310 K.

One should note that high energy Stark components' emission of the Er^{3+} $^4I_{13/2}$ level was used as a representative due to its large temperature sensitivity and, therefore, the highest relative sensitivity that can be obtained. Calculations based on overall Er^{3+} emission is given in ESI as Fig. S2.†

The Yb^{3+} ions bandshift and bandwidth change as thermometric parameters

Apart from the two LIR based temperature readout modes, another two thermometric parameters arise by considering only Yb^{3+} emission band ($^2F_{5/2} \rightarrow {}^2F_{7/2}$ transition): (a) significant
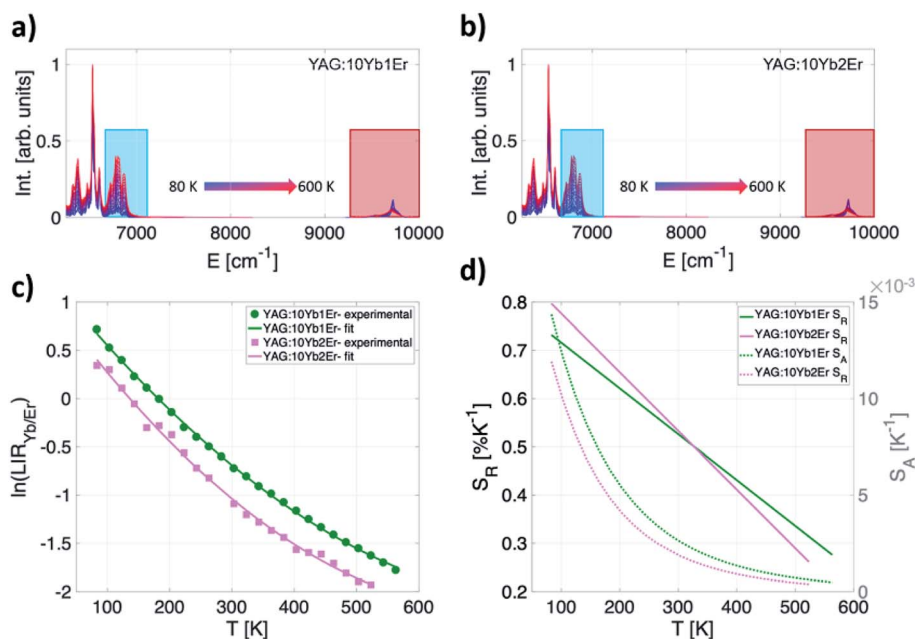

Fig. 3 Photoluminescence emission spectra of (a) YAG:10Yb1Er and (b) YAG:10Yb2Er samples. Thermometric properties of YAG:10Yb1Er (green line) and YAG:10Yb2Er (pink line) samples: (c) experimental (symbols) and theoretical (full line) temperature–dependent luminescence intensity ratio (ln(LIR$_{Yb/Er}$)), (d) S_A and S_R obtained by LIR$_{Yb/Er}$ readout.

a)

b)

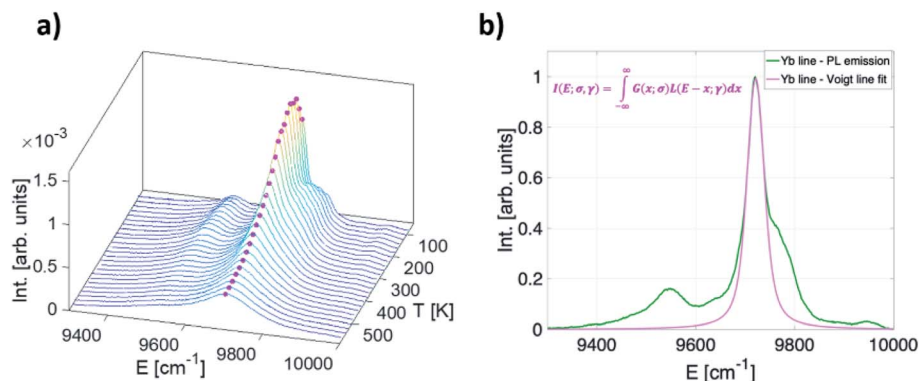$$I(E; \sigma, \gamma) = \int_{-\infty}^{\infty} G(x; \sigma) L(E - x; \gamma) dx$$

Fig. 4 (a) Temperature-dependant (80–600 K) photoluminescence emission spectra of Yb^{3+} in representative YAG:10Yb1Er (b) a Voigt line profile.

temperature-dependant redshift of the band maximum and (b) temperature-dependant band broadening (Fig. 4a). To investigate the thermally induced change of its position and full width half maximum (FWHM) change, the fit of the Yb^{3+} peak by the Voigt line profile was implemented (Fig. 4b).

The Voigt line form was chosen since it represents the convolution of Gaussian ($G(x; \sigma)$) and Lorentzian ($L(x; \gamma)$) line profiles hence being suitable to characterise the PL line shapes both at low and high temperatures:

$$I(E, \gamma) = \int_{-\infty}^{\infty} G(x; \sigma) L(E - x; \gamma) dx. \quad (9)$$

here, E is the position of the peak maximum, and σ (standard deviation) and γ (scale parameter) are parameters of Gaussian

and Lorentzian, respectively. Based on these fits, the position and FWHM band widths were obtained for all temperatures and are presented in Fig. 5a and b (symbols).

The fitting of experimental data to eqn (5) and (6) provided values of $\theta_D = 1092$ cm^{-1}, $\alpha = -347$ cm^{-1}, $\bar{\alpha} = 81$ cm^{-1}, $E^{inh} = 33$ cm^{-1} and $\theta_D = 999$ cm^{-1}, $\alpha = -287$ cm^{-1}, $\bar{\alpha} = 88$ cm^{-1}, $E^{inh} = 28$ cm^{-1}, for YAG:10Yb1Er and YAG:10Yb2Er samples, respectively.

Based on these fits, absolute sensitivities can be calculated for both samples for the bandshift (Fig. 5c) as well as for the FWHM (Fig. 5d). Relative sensitivity is also calculated and presented for the FWHM approach showing relatively high values for this type of measurements over the entire investigated temperature range having maximum of 0.46% K^{-1} at 210 K
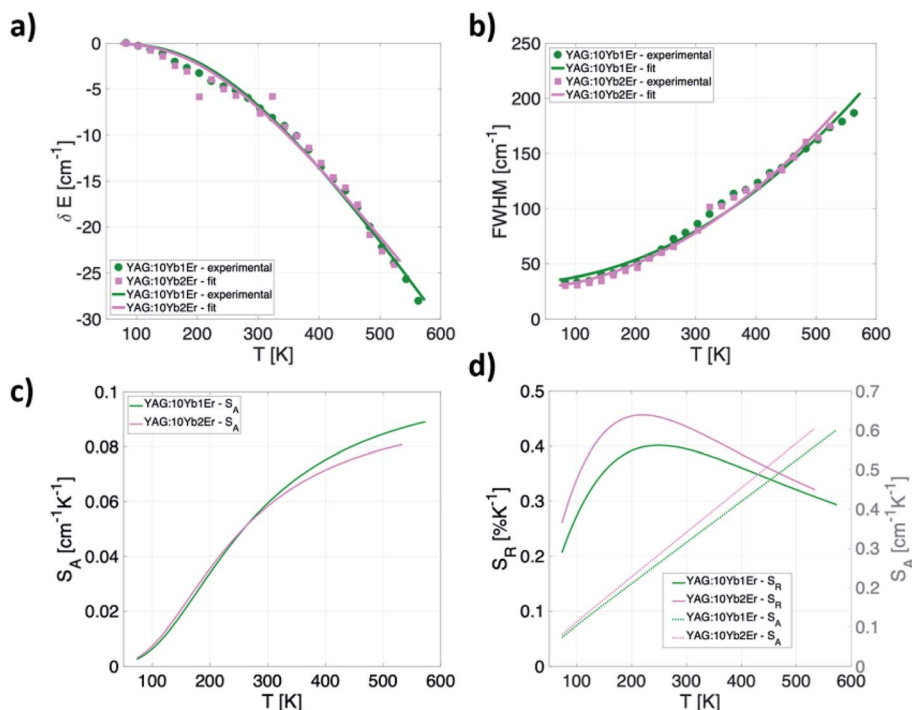

Fig. 5 Temperature dependences of (a) band shift; (b) FWHM; (c) absolute sensitivities obtained *via* band shift readout; (d) S_A and S_R obtained *via* FWHM readout for YAG:10Yb1Er and YAG:10Yb2Er samples.

Table 1 Comparison of S_A values for bandshift of different Ln^{3+} activated phosphors

Sample	S_A (cm^{-1} K^{-1})	Temperature range [K]	Ref.
YAG10Yb1Er	0.09	80–600	This work
YAG10Yb2Er	0.08	80–600	This work
YVO$_4$:Dy^{3+}	0.13@RT	RT–733	53
YVO$_4$:Eu^{3+}	0.20@RT	293–733	53
Y$_2$O$_2$S:Eu^{3+}	0.04	257–345	54
SrTiO$_3$:Eu^{3+}	0.03	4–420	55

obtained for the YAG:10Yb2Er sample (Fig. 5d). The S_R values for the band-shift readout are not presented since that can be a deceptive result, and it is in fact the S_A with maximum of 0.09 cm^{-1} K^{-1} at 575 K for the YAG:10Yb1Er sample represents more important figure of merit that limits temperature resolution. In the physiological relevant temperature range (303–333 K), this readout shows sensitivity of around 0.06 cm^{-1} K^{-1} at 310 K that may be considered as a good value when compared to the bandshift of other Ln^{3+} activated phosphors used for luminescence thermometry, Table 1.

Readout based on the kinetics of the $^2F_{5/2}$ state of Yb^{3+} ions

Finally, the methodology for the last temperature readout mode is based on the measurements of the Yb^{3+} emission lifetime. Here, the temperature dependence of the lifetime for both Yb^{3+}/Er^{3+} co-doped samples (YAG:10Yb1Er and YAG:10Yb2Er) as well as for the sample singly doped with Yb^{3+} (YAG:10Yb) are presented in the Fig. 6a.

As can be seen, when co-doped with Er^{3+} ions, Yb^{3+} $^2F_{5/2} \rightarrow$ $^2F_{7/2}$ emission lifetimes are significantly suppressed. The suppression of the lifetime indicates well known energy transfer (ET) process between Yb^{3+} and Er^{3+} ions. As a measure of the transfer, a value of relative change in the lifetime of Yb^{3+}/Er^{3+} doped samples compared to only Yb^{3+} doped one can be used and energy transfer is calculated in accordance with:

$$ET = \frac{\tau_{Yb} - \tau_{Yb,Er}}{\tau_{Yb}} = 1 - \frac{\tau_{Yb,Er}}{\tau_{Yb}}, \qquad (10)$$

where τ_{Yb} and $\tau_{Yb,Er}$ represent lifetimes of $^2F_{5/2}$ state for the sample only doped with Yb^{3+} and co-doped with Yb^{3+}, Er^{3+} ions, respectively. Determined values for both YAG:10Yb1Er and YAG:10Yb2Er samples were exceedingly high (approximately 80%) and they are temperature independent (Fig. 6b).

Considering the temperature independence of energy transfer process, the thermal evolution of the $^2F_{5/2}$ lifetime for both YAG:10Yb1Er and YAG:10Yb2Er samples was measured and the results are presented in Fig. 7a. Observed unusual rise followed by the drop in the lifetime values can be contributed to the self-trapping mechanism known to exist in YAG: Yb^{3+}.[56] Semi-empirical formula was proposed to fit the experimental data (full lines on the Fig. 7a):

$$\tau(T) = \tau_0 \frac{1 + C_2 \exp\left(-\dfrac{\Delta E_2}{kT}\right)}{1 + C_1 \exp\left(-\dfrac{\Delta E_1}{kT}\right)}, \qquad (11)$$

where τ_0 is the radiative lifetime, ΔE_1 and ΔE_2 are the activation energies of the thermal quenching process and radiative trapping process, respectively, while C_1 and C_2 are fitting constants.

This semiempirical model (eqn (11)) provided the fitting parameters for YAG:10Yb1Er and YAG:10Yb2Er of $\tau_0 = 131$ μs, $C_1 = 6.202$, $\Delta E_1 = 604$ cm^{-1}, $C_2 = 3.381$, $\Delta E_2 = 253$ cm^{-1} and $\tau_0 = 124$ μs, $C_1 = 7.330$, $\Delta E_1 = 648$ cm^{-1}, $C_2 = 3091$, $\Delta E_2 = 309$ cm^{-1}, respectively, Fig. 7b represents calculated S_A and S_R for both samples.

Due to the nonmonotonic dependence of the lifetime on temperature, two separate, non-overlapping temperature ranges of application are possible. The first application window covers temperatures from 80 K to 260 K with maximum relative sensitivity of 0.86% K^{-1} at 160 K for YAG:10Yb2Er sample.

Second window covers the temperatures above 260 K showing the maximum relative sensitivity around 390 K with value of 0.32% K^{-1} and around 0.23% K^{-1} in the physiological temperature range for the YAG:10Yb2Er sample.

The values of maximal relative sensitivities and sensitivities in the physiological temperature range obtained by investigated all NIR temperature readouts are summarized in Table 2.
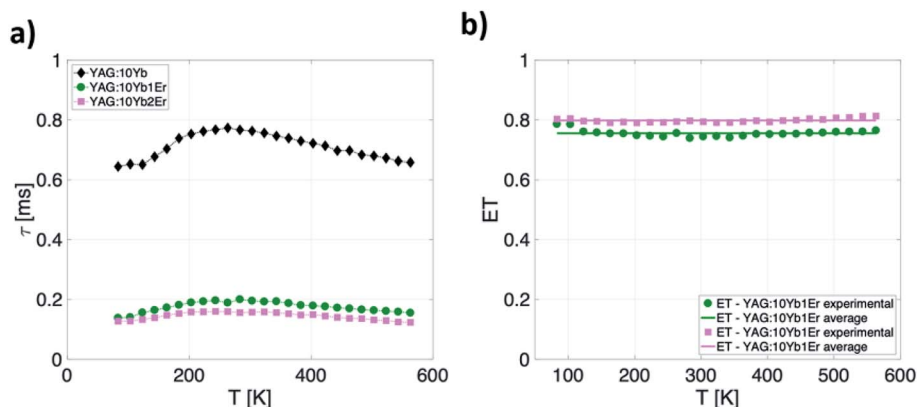

Fig. 6 (a) Temperature dependence of the $^2F_{5/2}$ lifetime for YAG:10Yb1Er, YAG:10Yb2Er and YAG:10Yb samples and (b) temperature-dependence of Yb$^{3+} \rightarrow$ Er^{3+} energy transfer.
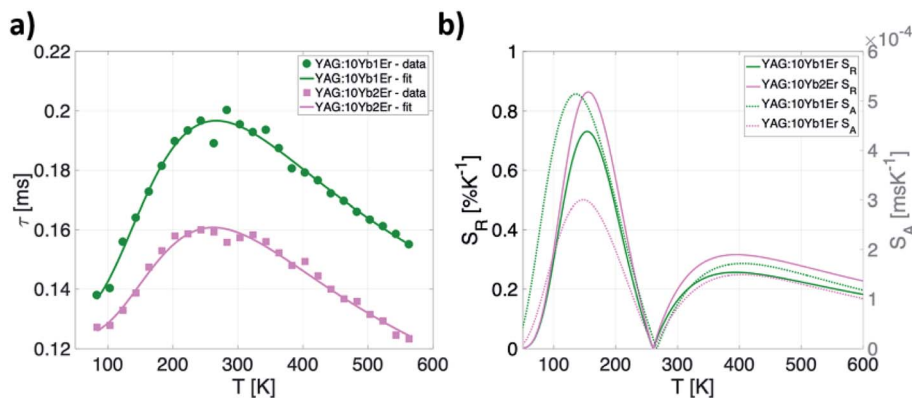
Fig. 7 (a) Temperature dependence of emission lifetime values and (b) calculated absolute and relative sensitivities for YAG:10Yb1Er and YAG:10Yb2Er samples.

Table 2 Summarized S_R values for 4 NIR readouts obtained with YAG: Yb^{3+}, Er^{3+} nanoparticles

Readout	SRmax (% K^{-1})		S_R (% K^{-1})@310 K	
	YAG10Yb1Er	YAG10Yb2Er	YAG10Yb1Er	YAG10Yb2Er
LIR$_{Er/Er}$	1@163 K	1@163 K	0.3	0.3
LIR$_{Yb/Er}$	0.73@83 K	0.80@83 K	0.5	0.5
FWHM	0.40@249 K	0.46@201 K	0.39	0.43
LT	0.73@154 K	0.86@156 K	0.19	0.23

The reproducibility of temperature:

$$R_p = \left(1 - \frac{\max|T_i - T_j|}{T_i}\right) \times 100\%, \qquad (12)$$

determined by these four different readouts from luminescence is higher than 98% at 300 K (i and j stand for different temperature readouts), suggesting the excellent cross-validation of thermometry results. Therefore, this nanothermometer can be used with different luminescence thermometry setups operating with different temperature readouts. In addition, different principles of temperature readings may be exploited for the cross-calibration to reduce systematic errors in measurements as well as to eliminate artifacts associated with the interaction of the measurement probe with the environment.

Conclusion

Beside conventional Er^{3+}-based LIR methods that utilize visible emissions, the Er^{3+} activator emissions can be exploited for the luminescence thermometry in biological transparency windows alone or in combination with Yb^{3+} emission. The small energy difference between Stark components of the Er $^4I_{13/2}$ levels is reflected in moderate but sufficient values of the readout sensitivities in the physiological temperature range. On the other hand, the small energy difference is beneficial for LIR thermometry since it ensures thermalization between energy levels over the wide temperature range. The good sensitivities at low temperatures open possibilities for the sensitive thermometry especially in environments compromised by visible background absorption, scattering and luminescence. Since temperature can be measured by four different approaches, all utilizing NIR excitation and emissions, it is possible to employ any existing temperature readout scheme, and to exploit the multi-readout approach with two or more combined readouts to improve precision and reliability of measurements. When compared to intensities of up-conversion emissions that are most used for the Er^{3+} luminescence thermometry, the down-shifting emissions exploited here in all 4 readout approaches are of considerably higher intensities which presents an additional benefit to thermometry.

Author contributions

Conceptualization, M. D. Dramićanin; data curation, J. Periša, W. Piotrowski.; formal analysis, J. Periša, Z. Ristić, W. Piotrowski, Ž. Antić, L. Marciniak, M. D. Dramićanin; visualization, J. Periša, Z. Ristić, L. Marciniak; methodology, M. D. Dramićanin, L. Marciniak, Ž. Antić; writing-original draft, J. Periša, Z. Ristić, Ž. Antić; writing-review and editing, M. D. Dramićanin, L. Marciniak.

Conflicts of interest

There are no conflicts to declare.

References

1 M. Dramićanin, *Luminescence Thermometry*, Elsevier Science, Cambridge, United Kingdom, 1st edn, 2018, pp. 113–157.

2 D. Jaque and F. Vetrone, *Nanoscale*, 2012, **4**, 4301.

3 C. D. S. Brites, S. Balabhadra and L. D. Carlos, *Adv. Opt. Mater.*, 2019, **7**, 1801239.

4 M. Dramićanin, *J. Appl. Phys.*, 2020, **128**, 040902.

5 X. Lin, M. Kong, N. Wu, Y. Gu, X. Qiu, X. Chen, Z. Li, W. Feng and F. Li, *ACS Appl. Mater. Interfaces*, 2020, **12**, 52393–52401.

6 M. Quintanilla and L. M. Liz-Marzán, *Nano Today*, 2018, **19**, 126–145.

7 M. Tan, F. Li, N. Cao, H. Li, X. Wang, C. Zhang, D. Jaque and G. Chen, *Small*, 2020, 2004118.

8 J. Zhou, B. del Rosal and D. Jaque, *Nat. Methods*, 2020, **17**, 967–980.

9 B. del Rosal, E. Ximendes, U. Rocha and D. Jaque, *Adv. Opt. Mater.*, 2016, **5**, 1600508.

10 M. Suta, Ž. Antić, V. Đorđević, S. Kuzman, M. D. Dramićanin and A. Meijerink, *Nanomaterials*, 2020, **10**, 543.

11 X. Xu, Z. Wang, P. Lei, Y. Yu, S. Yao, S. Song, X. Liu, Y. Su, L. Dong, J. Feng and H. Zhang, *ACS Appl. Mater. Interfaces*, 2015, **7**, 20813–20819.

12 A. M. Smith, M. C. Mancini and S. Nie, *Nat. Nanotechnol.*, 2009, **4**, 710.

13 E. Hemmer, A. Benayas, F. Légaré and F. Vetrone, *Nanoscale Horiz.*, 2016, **1**, 168.

14 A. M. Kaczmarek, M. Suta, H. Rijckaert, A. Abalymov, I. Van Driessche, A. G. Skirtach, A. Meijerink and P. Van Der Voort, *Adv. Funct. Mater.*, 2020, **30**, 2003101.

15 S. He, J. Song, J. Qu and Z. Cheng, *Chem. Soc. Rev.*, 2018, **47**, 4258.

16 E. Hemmer, N. Venkatachalam, H. Hyodo, A. Hattori, Y. Ebina, H. Kishimoto and K. Soga, *Nanoscale*, 2013, **5**, 11339–11361.

17 I. E. Kolesnikov, A. A. Kalinichev, M. A. Kurochkin, E. V. Golyeva, E. Yu Kolesnikov, A. V. Kurochkin, E. Lahderanta and M. D. Mikhailov, *Sci. Rep.*, 2017, **7**, 18002.

18 M. Kamimura, T. Matsumoto, S. Suyari, M. Umezawa and K. Soga, *J. Mater. Chem. B*, 2017, **5**, 1917–1925.

19 I. Porosnicu, C. Colbea, F. Baiasu, M. Lungu, M. Cosmin Istrate, D. Avram and C. Tiseanu, *Methods Appl. Fluoresc.*, 2020, **8**, 035005.

20 M. Ji, Z. Fu, G. Liu, Z. Sun, P. Li, A. Zhang, F. Lin, B. Hou and G. Chen, *Adv. Opt. Mater.*, 2020, 1901173.

21 W. Xu, Y. Hu, L. Zheng, Z. Zhang, W. Cao, H. Liu and X. Wu, *J. Lumin.*, 2019, **208**, 415–423.

22 L. Marciniak, A. Bednarkiewicz and K. Elzbieciak, *J. Mater. Chem. C*, 2018, **6**, 7568–7575.

23 L. Marciniak, K. Prorok, A. Bednarkiewicz, A. Kowalczyk, D. Hreniak and W. Strek, *J. Lumin.*, 2016, **176**, 144–148.

24 C. Hazra, A. Skripka, S. J. L. Ribeiro and F. Vetrone, *Adv. Opt. Mater.*, 2020, **8**, 2001178.

25 M. D. Dramićanin, *Methods Appl. Fluoresc.*, 2016, **4**, 042001.

26 W. Piotrowski, K. Trejgis, K. Maciejewska, K. Ledwa, B. Fond and L. Marciniak, *ACS Appl. Mater. Interfaces*, 2020, **12**, 44039–44048.

27 A. Bednarkiewicz, L. Marciniak, L. D. Carlos and D. Jaque, *Nanoscale*, 2020, **12**, 14405–14421.

28 P. Cortelletti, A. Skripka, C. Facciottia, M. Pedroni, G. Caputo, N. Pinna, M. Quintanilla, A. Benayas, F. Vetrone and A. Speghini, *Nanoscale*, 2018, **10**, 2568–2576.

29 S. Goderski, M. Runowski, P. Woźny, V. Lavín and S. Lis, *ACS Appl. Mater. Interfaces*, 2020, **12**, 40475–40485.

30 M. Runowski, N. Stopikowska, D. Szeremeta, S. Goderski, M. Skwierczyńska and S. Lis, *ACS Appl. Mater. Interfaces*, 2019, **11**, 13389–13396.

31 C. D. S. Brites, A. Millán and L. D. Carlos, Chapter 281-Lanthanides in Luminescent Thermometry, in *Handbook on the Physics and Chemistry of Rare Earths*, ed. B. Jean-Claude and K. Pecharsky Vitalij, Elsevier, 2016, vol. 49, pp. 339–427.

32 M. Runowski, A. Shyichuk, A. Tymiński, T. Grzyb, V. Lavín and S. Lis, *ACS Appl. Mater. Interfaces*, 2018, **10**, 17269–17279.

33 M. Runowski, S. Goderski, D. Przybylska, T. Grzyb, S. Lis and I. R. Martín, *ACS Appl. Nano Mater.*, 2020, **3**, 6406–6415.

34 E. C. Ximendes, U. Rocha, T. O. Sales, N. Fernández, F. Sanz-Rodríguez, I. R. Martín, C. Jacinto and D. Jaque, *Adv. Funct. Mater.*, 2017, **27**, 1702249.

35 D. Avram, I. Tiseanu, B. S. Vasile and C. Tiseanu, *Sci. Rep.*, 2018, **8**, 18033.

36 M. Haase and H. Schafer, *Angew. Chem., Int. Ed.*, 2011, **50**, 5808–5829.

37 D. Hreniak and W. Strk, *J. Alloys Compd.*, 2002, **341**, 183–186.

38 M. P. Pechini, *US Pat.* 3330697, 1967.

39 A. V. Belyakov and N. A. Kulikov, *Refract. Ind. Ceram.*, 2011, **52**, 61–62.

40 A. Jain, P. Sengar and G. A. Hirata, *J. Phys. D: Appl. Phys.*, 2018, **51**, 303002.

41 A. Ćirić, J. Aleksić, T. Barudžija, Ž. Antić, V. Đorđević, M. Medić, J. Periša, I. Zeković, M. Mitrić and M. D. Dramićanin, *Nanomaterials*, 2020, **10**, 627.

42 D. E. McCumber and M. D. Sturge, *J. Appl. Phys.*, 1963, **34**, 1682–1684.

43 W. M. Yen and W. C. Scott, *Phys. Rev. [Sect.] A*, 1964, **136**, A271–A283.

44 C. C. Klick and J. H. Schulman, Luminescence in Solids, in *Solid State Physics*, ed. F. Seitz and D. Turnbull, Academic Press, 1957, vol. 5, pp. 97–172.

45 T. Senden, R. J. A. van Dijk-Moes and A. Meijerink, *Light: Sci. Appl.*, 2018, **7**, 8.

46 R. D. Shannon, *Acta Crystallogr., Sect. A: Cryst. Phys., Diffr., Theor. Gen. Crystallogr.*, 1976, **A32**, 751–767.

47 D. Rodic, M. Mitric, R. Tellgren and H. J. Rundlof, *J. Magn. Magn. Mater.*, 2001, **232**, 1.

48 J. Periša, J. Papan, S. D. Dolić, D. J. Jovanović and M. D. Dramićanin, *Dyes Pigm.*, 2018, **155**, 233–240.

49 I. O. Vorona, R. P. Yavetskiy, A. G. Doroshenko, S. V. Parkhomenko, V. N. Baumer, A. V. Tolmachev, D. Yu Kosyanov, V. I. Vovna, V. G. Kuryavyi, M. Greculeasa, L. Gheorghe, S. Hau, C. Gheorghe and G. Croitoru, *J. Eur. Ceram. Soc.*, 2017, **37**, 4115–4122.

50 F. Tang, Y. Cao, W. Guo, Y. Chen, J. Huang, Z. Deng, Z. Liu and Z. Huang, *Opt. Mater.*, 2011, **33**, 1278–1282.

51 Q. Zhan, J. Qian, H. Liang, G. Somesfalean, D. Wang, S. He and Z. Zhang, *ACS Nano*, 2011, **5**, 3744–3757.

52 H. Fritsche, O. Lux, C. Schuett, S. W. Heinemann, M. Dziedzina, W. Gries and H. J. Eichler, *Proc. SPIE 8959, Solid State Lasers XXIII: Technology and Devices*, 2014, p. 895907.

53 A. Ćirić, S. Stojadinović and M. D. Dramićanin, *Sens. Actuators, A*, 2019, **295**, 450.

54 H. Kusama, O. J. Sovers and T. Yoshioka, *Jpn. J. Appl. Phys.*, 1967, **15**, 2349.

55 M. Lüders and K. F. Renk, *Solid State Commun.*, 1969, **7**, 575.

56 G. Boulon, L. Laversenne, C. Goutaudier, Y. Guyot and M. T. Cohen-Adad, *J. Lumin.*, 2003, **102–103**, 417–425.